

# Cantilever Micromachined Structures in CMOS Technology with Magnetic Actuation

Bing Shen<sup>1</sup>, Walter Allegretto<sup>2</sup>, Yuan Ma, Bing Yu,  
Ming Hu<sup>3</sup> and Alexander M. Robinson

Electrical Engineering Department and the Alberta Microelectronic Centre,  
University of Alberta, Edmonton, Alberta, Canada T6G 2G7

(Received May 30, 1996; accepted September 16, 1996)

**Key words:** magnetic actuation, CMOS, micromachining, nested cantilevers, angular deflection

We have designed and tested a CMOS-compatible magnetically actuated micromachined cantilever device. The structure involves nested cantilevers to enhance the angular deflection of the inner cantilever. Deflections of  $\pm 1.5^\circ$  under static operation and  $\pm 27^\circ$  under resonant dynamic conditions were measured. The paper includes a comparison of experimental measurements with an analytic and numerical analysis of the device.

## 1. Introduction

CMOS-compatible micromachining is now accepted as a viable method for fabricating microsensors.<sup>(1–24)</sup> Until recently, however, most of the research and development has concentrated on the investigation of static devices, composed of fixed two- or three-dimensional mechanical microstructures that function with little spatial displacement. Whether CMOS-compatible micromachining has a place in the growing area of dynamic structures using standard processes may depend on finding a suitable force to actuate the mechanical movement.

The previous comments are not meant to imply that no movable microstructures have been fabricated using a CMOS process. A subnanogram discrete mass resonant biosensor cantilever fabricated in a standard  $1.2\ \mu\text{m}$  CMOS process has been reported,<sup>(10,19)</sup> in which vibrations externally applied to the die resulted in resonant oscillation of the cantilever at a frequency dependent on the discrete mass placed on the cantilever. Thermal actuation of a

---

<sup>1</sup> Now at GE Medical Systems, Milwaukee, WI, USA.

<sup>2</sup> Department of Mathematical Sciences, University of Alberta.

<sup>3</sup> On leave from the Department of Electrical Engineering, Tianjin University, Tianjin, China.

cantilever was reported in one of the original papers on CMOS micromachining,<sup>(5,6)</sup> whose operating principle is based on two material layers of different thermal expansion coefficients. This technique was improved recently<sup>(20)</sup> and has now been somewhat refined and thoroughly analyzed for a micromirror cantilever.<sup>(25,26)</sup>

In this paper, we describe a magnetically actuated CMOS-compatible micromachined cantilever device capable of a large angular deflection. Actuation is produced by Lorentz forces due to interaction between currents flowing in the cantilever and an external magnetic field. This device is unique in several ways: magnetic actuation has not been applied to a CMOS-fabricated device before; because of the volume micromachining and the magnetic actuation, symmetric bi-directional displacement is possible; and the cantilever design employs the concept of multiple nested cantilevers to enhance the angular deflection of the inner cantilever.

The paper includes an analytic and a numerical analysis of the cantilever-in-cantilever structure, comparison of experimental measurements with analysis of both static and dynamic operation, and also comparison of numerical simulation with experiment. The cantilever devices give a rotation of  $\pm 1.5^\circ$  under static operation and  $\pm 27^\circ$  under resonant dynamic operation.

## 2. Device Design and Construction

A plan view of a simple cantilever structure for a magnetically actuated mirror is shown in Fig. 1. The electrical lead and the direction of the applied magnetic field are also indicated. For the configuration shown in the figure, there will be a Lorentz force along the length  $l$  of the wire at the end of the cantilever, bending the structure out of the plane of the figure. A reverse current will bend the structure in the opposite direction.

The structure is similar to the thermally actuated micromirror referred to previously.<sup>(25,26)</sup> The device consists of two parallel cantilever arms supporting the mirror plate between their tips. The region of minimum contact between the ends of the cantilever arms and the mirror reduces the bending load on the arms and also keeps the mirror surface flat when the cantilevers bend. We call this basic structure with one pair of cantilever arms a single cantilever-in-cantilever (CIC) device.

A SEM of a triple CIC device is shown in Fig 2(a). The central mirror cantilever is embedded in the surrounding cantilever which, in turn, is embedded sequentially in two other surrounding but opposite-facing cantilevers. Some slight inherent stress in the structure is evident in the figure. The central cantilever mirror has dimensions  $150 \mu\text{m}$  wide by  $200 \mu\text{m}$  long and all the cantilever arms are  $12 \mu\text{m}$  wide; the anisotropically etched pit has dimensions  $350 \mu\text{m}$  by  $290 \mu\text{m}$  at the substrate surface, and a depth of approximately  $50 \mu\text{m}$ .

This particular device was fabricated by Northern Telecom Canada Ltd. using its  $1.2 \mu\text{m}$  CMOS process. We followed with an anisotropic etch to release the structure. The standard metal1 and metal2 layers (Al) of the CMOS process are suitably routed to conduct current around the peripheries of all but the central cantilever. The layout of the metal leads is schematically shown in Fig. 2(b), along with dimensions of the triple CIC structure. The

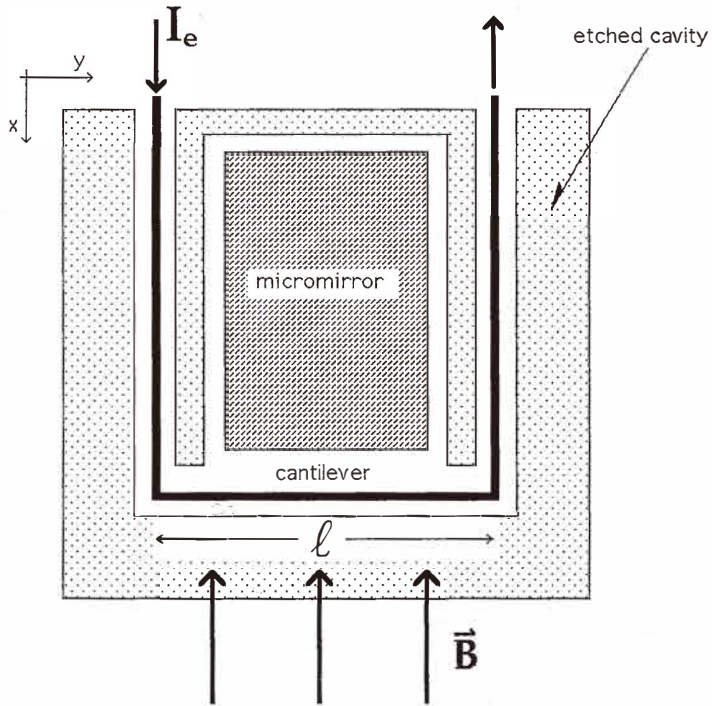


Fig. 1. Simple (single) cantilever structure for a magnetically actuated mirror.

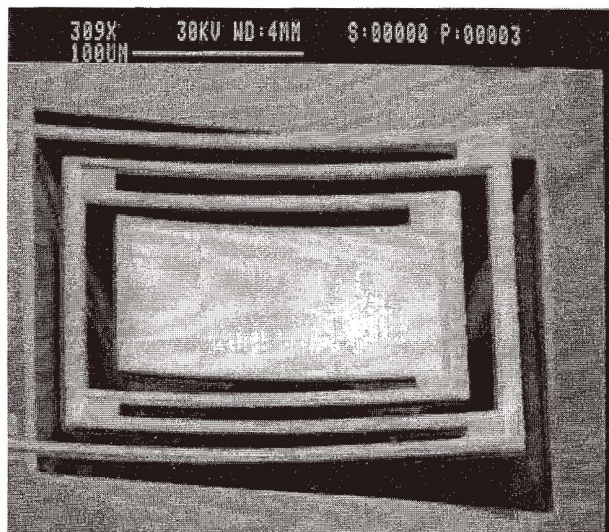


Fig. 2(a). SEM of a triple CIC device.

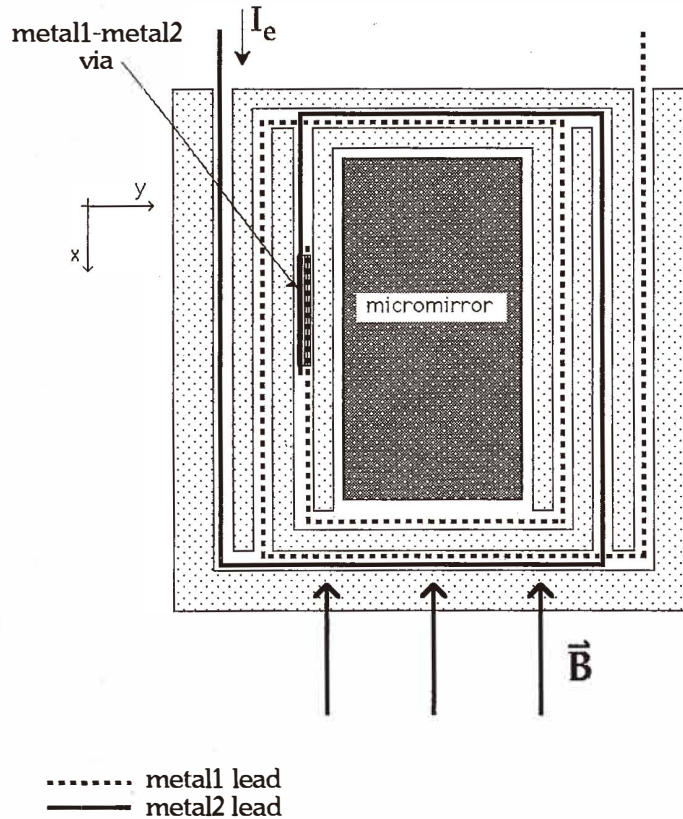


Fig. 2(b). Plan view of a triple CIC device showing arrangement of the Al leads. In regions where the leads are side-by-side, they actually overlap. View is not drawn to scale.

leads are  $6 \mu\text{m}$  wide. In the regions where they are shown side by side in the diagram, the metal1 layer actually overlays the metal2 layer; they are electrically insulated by the intermetal oxide layer of the CMOS process. The metal leads are arranged in such a pattern that the generated Lorentz forces on the two ends of any cantilever always have opposite directions.

### 3. Static Cantilever Deflection Analysis

An analytic expression for the static displacement and angular deflection of our CIC devices can be obtained if we adopt a simplifying model where we neglect any bending of the cantilever in the transverse direction, assume the Lorentz force is split equally into two

point forces, each acting at the ends of the cantilever arms, and decompose the CIC structure into separate cantilevers. We then apply the standard equations<sup>(27)</sup> for the displacement and deflection angle at the ends of sequential cantilevers, with the boundary conditions obtained by matching deflection and loads at each end with those of the previous cantilever.

The analysis for a CIC structure containing  $n$  cantilevers is given in detail in ref. 28; for the triple CIC, the displacement  $Z_{max}$  and deflection angle  $\theta$  of the base of the mirror plate, that is, the innermost Al lead, is given by the following two equations:

$$Z_{max} = Z_{max1} - Z_{max2} + Z_{max3}$$

$$= \frac{P_1 L_1^3 - (P_2 - P_1) L_2^3 + [P_3 - (P_2 - P_1)] L_3^3}{3EI} + \frac{-P_1 L_1 L_2^2 + [P_1 L_1 + (P_2 - P_1) L_2] L_3^2}{2EI}$$

$$\theta = \theta_1 + \theta_2 + \theta_3$$

$$= \frac{P_1 L_1^2 + (P_2 - P_1) L_2^2 + [P_3 - (P_2 - P_1)] L_3^2}{2EI} + \frac{P_1 L_1 L_2 + [P_1 L_1 + (P_2 - P_1) L_2] L_3}{EI}$$

where  $F_1 = P_1$  = the Lorentz force generated at the end of each arm of the innermost "active" cantilever,

$F_i = P_i - F_{i-1}$  for  $i = 2, 3$  is the net force acting on each arm of the  $i$ -th innermost cantilever,

$P_i$  = the Lorentz force at the end of each arm of the same cantilever,

$L_i$  = the arm length of cantilever  $i$ ,

$E$  = Young's modulus of the material forming the cantilever arms, and

$I$  = moment of inertia about the neutral axis of the cross section of the cantilever arms, with each cantilever having identical cross sections.

The conclusions drawn from these static equations are summarized as follows:

- The vertical displacements of any two successive cantilevers are always in opposite directions, while the rotation angles of all the cantilevers contribute in the same direction.
- The total deflection is proportional to the magnetic field intensity  $B$  and electric current  $I_e$ .
- The maximum moment occurs at the fixed ends of the outer cantilever, as do the highest stresses and strains. Thus these ends represent good locations to place piezoresistive sensors.
- The more embedded cantilevers there are, the greater the attainable angular deflection.

To calculate values of deflection and rotation for comparison between a single and triple CIC structure, consider the following geometric and operating conditions for the structures shown in Figs. 1 and 2(a). For  $I_e = 10$  mA,  $B = 0.1$  T, and for the single cantilever,  $l = 200$   $\mu\text{m}$ ,  $L = 180$   $\mu\text{m}$ , the total Lorentz force  $F = I_e l B = 0.2$   $\mu\text{N}$ . Assuming half of that force is acting on each cantilever arm of width  $12$   $\mu\text{m}$ , the equations predict:

$$\theta = 0.033^\circ \text{ and } Z_{max} = 0.055 \mu\text{m}.$$

On the other hand, for the triple CIC, which has the same central cantilever dimensions, and  $L_1 = L = 180 \mu\text{m}$ ,  $L_2 = 208 \mu\text{m}$  and  $L_3 = 236 \mu\text{m}$ , we get  $P_1 = 0.1 \mu\text{N}$ ,  $P_2 = 0.228 \mu\text{N}$  and  $P_3 = 0.284 \mu\text{N}$  so that  $\theta = 0.38^\circ$  and  $Z_{\text{max}} = 0.38 \mu\text{m}$ .

Thus, the calculations show the triple CIC design has enhanced the rotation by more than 10 times.

#### 4. Dynamic Numerical Simulation

The static cantilever deflection analysis cannot be readily adapted to obtain a description of the dynamic behavior. Instead, we utilize numerical simulation, as follows.

The deflection  $z$  of the device is assumed to be governed by the classical equations of linear elasticity,<sup>(29)</sup> and specifically:

$$\rho \frac{\partial^2 z}{\partial t^2} + \rho_1 \frac{\partial z}{\partial t} + Lz = q(x, y, t)$$

$$\text{with: } L(z) = \frac{\partial^2}{\partial x^2} \left[ D_x \frac{\partial^2 z}{\partial x^2} \right] + \frac{\partial^2}{\partial y^2} \left[ D_y \frac{\partial^2 z}{\partial y^2} \right] \\ + \frac{\partial^2}{\partial y^2} \left[ D_1 \frac{\partial^2 z}{\partial x^2} \right] + \frac{\partial^2}{\partial x^2} \left[ D_1 \frac{\partial^2 z}{\partial y^2} \right] + 2 \frac{\partial^2}{\partial x \partial y} \left[ D_{xy} \frac{\partial^2 z}{\partial x \partial y} \right]$$

subject to the usual boundary conditions.

Here,  $D_x(x, y)$ ,  $D_y(x, y)$ ,  $D_1(x, y)$ ,  $D_{xy}(x, y)$  denote the flexural rigidities of the device,  $\rho$  the area density (mass/area),  $\rho_1$  the damping term and  $q$  the load. These parameters are calculated as indicated in ref. 29 using the bulk values of the material. Specifically, we set the volume density at  $3.0 \times 10^{-15} \text{ kg}/\mu\text{m}^3$  for the nitride layers and  $2.3 \times 10^{-15} \text{ kg}/\mu\text{m}^3$  for the other layers; Young's modulus  $E$  is set at  $320 \times 10^{-3} \text{ N}/\mu\text{m}^2$  for the nitride and  $74 \times 10^{-3} \text{ N}/\mu\text{m}^2$  for the other materials and Poisson's ratio  $\nu$  is chosen to be 0.1025. The thicknesses of the CMOS materials are set at  $0.4 \mu\text{m}$  for the nitride layer,  $0.8 \mu\text{m}$  for each metal layer and  $2.4 \mu\text{m}$  for the other layers. The final values of the equation parameters are then obtained by integration over the device thickness.

We are restricted to using bulk values of the parameters because values pertaining to material films are not generally available. Possible differences in the values are not expected to be large, and should not affect the simulations significantly.

The equation for  $L$  was discretized by a finite element procedure using the classical macrotriangle approach.<sup>(30)</sup> The resonant frequencies were calculated by first neglecting the damping term  $\rho_1$  and calculating the eigenvalues (and eigenvectors) of  $L$  using a routine iteration procedure.<sup>(30)</sup> Subsequent calculation of  $\rho_1$  from experimental results indicates that our procedure is well justified since  $\rho_1^2 / (\rho \lambda_1)$  is less than  $10^{-3}$ , where  $\lambda_1$  denotes the

first eigenvalue of the CIC structure. Because the geometry of the Al leads in the device was designed for flexure of the cantilever in the plane of symmetry, the nature of the loads generated by the Lorentz forces implies that some of the possible CIC eigenfrequencies will not be readily excited.

## 5. Experiment

We investigated double and triple CIC devices. The double CIC device is similar to the triple shown in Fig. 2(a), except that it does not have the outer surrounding cantilever. The simple experimental setup is shown in Fig. 3. The die with the devices is placed between the poles of a permanent magnet, with a magnetic field intensity of 0.12T in the direction indicated in Fig. 1. The beam from a HeNe laser is focused on the center of the cantilever mirror and the reflected beam falls on an opaque screen or a photodetector. The angle of the central cantilever is determined by the position of the reflected laser beam. The curvature of the mirror apparent in Fig. 2(a), due to the inherent stress, places further divergence in the optics. The reflected beam has a diameter of approximately 10 mm on the screen, and limits the precision of the angular measurement to approximately  $0.15^\circ$ .

To eliminate the effects of unidirectional deflections due to inherent stress or thermal actuation, the total cantilever tilt produced upon reversing the direction of current was measured by observing the change in extreme positions of the reflected laser beam. To measure the response time, a photodiode was used instead of the opaque screen. DC,

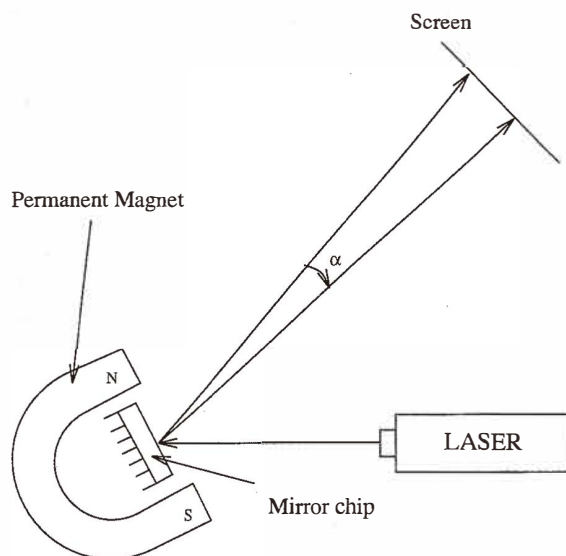


Fig. 3. Experimental setup for measuring micromirror deflection.

square and sine wave AC currents were applied to determine the static and dynamic response of the devices. For the AC measurements at frequencies above a few Hz, the reflected laser beam appears as a fan of light as the mirror oscillates.

## 6. Results and Discussion

### 6.1 Static response

Figure 4 indicates the measured tilt of the mirror for the two types of devices as a function of DC current. A typical error bar is shown to indicate the precision of the angular measurement quoted above. The deflection for both devices is linear with current, as predicted by the analytic expressions which are plotted as solid lines. They show excellent agreement with the experimental points. The triple CIC device shows a significantly larger deflection than the double, supporting our expectation that the cascaded CIC structure enhances the deflection of the central cantilever.

The limit to the current that can be passed through the structure is set by Joule heating of the Al leads in the cantilevers. Because the structure is thermally isolated due to the etching process, the temperature can readily increase to a high value. Using the bulk value of the temperature coefficient of resistance for Al, and measuring the resistance of the Al leads, the average temperature of the structure may be obtained. We find, for example, that a DC current of 20 mA will raise the cantilever support arms' average temperature to approximately 150°C above room temperature. We limit our current so the average temperature remains below 300°C, and for the triple CIC device, this amounts to approximately 25 mA.

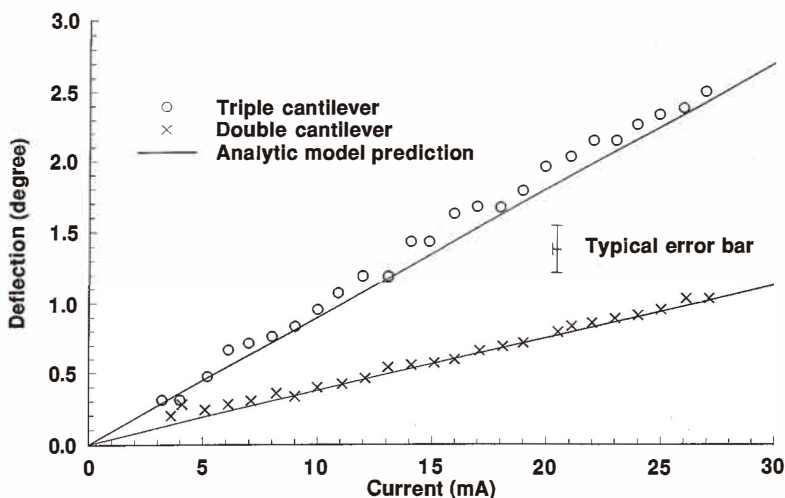


Fig. 4. Static micromirror deflection as a function of current for double and triple CIC devices.

## 6.2 Time response

The time response of a triple CIC was measured using an EG & G UV444BQ photodiode which has a photosensitive surface diameter of 11 mm. The detector was placed so that the reflected laser beam partially overlapped the detector surface. When a step function current pulse was applied to the CIC device, more or less of the beam deflected onto the detector, giving an increase or reduction in signal. On applying a 100 Hz symmetric square wave current, the resultant signal suggested that the movement of the mirror can be regarded as a damped free vibration. The structure had a measured response time of approximately 28  $\mu$ s and damps out in approximately 2.5 ms. The response was not exactly that of a single exponential decaying harmonic oscillation, but rather, showed a beating effect, presumably due to higher-order vibrations.

## 6.3 Resonant response

The frequency response near resonance was measured using the same experimental setup for the static deflection measurements. Symmetric square wave AC currents were applied to excite the oscillations. The spread angle of the fan-shaped reflected laser beam varied with frequency and magnitude of the input current. The variation of the tilt of a triple CIC device versus the frequency near 17 kHz at different amplitudes of AC current is plotted in Fig. 5. The maximum deflections are approximately 10°, 16° and 20° for the three lower currents; at 10 mA, the fan-shaped beam of reflected light became asymmetric at resonance, as is its response curve. We attribute this to the central cantilever striking the bottom of the etched pit beneath it, limiting its deflection to 25°. This limitation is as expected from simple geometric considerations. The resonant frequency is 16.9 kHz, and the Q of the vibrating structure is approximately 35. The double cantilever shows a similar

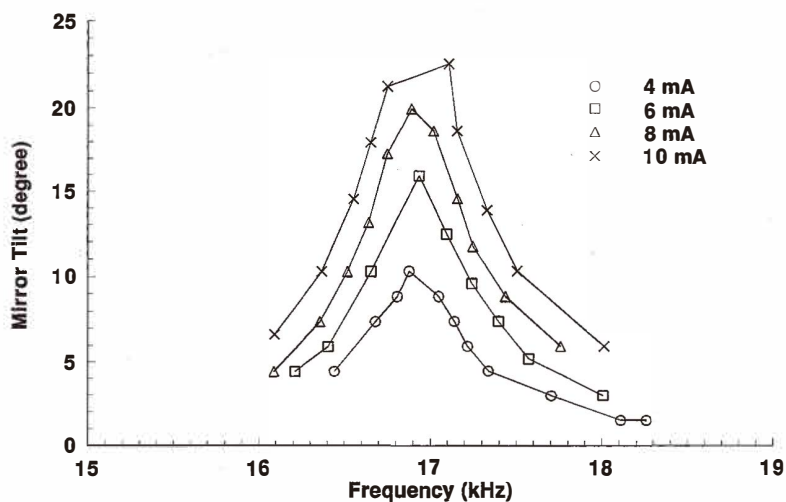


Fig. 5. Resonance curves for a triple CIC device at the second resonance frequency for various currents.

response, but with a smaller deflection, amounting to approximately 75% of the triple device. The resonant frequency and the Q were approximately 25.3 kHz and 90, respectively. Apparently the frequency and Q are higher for the double CIC because it is smaller.

The results discussed above are at the frequency at which the greatest angular deflection occurs, which for our device is the second harmonic, as discussed below. Table 1 lists the response of another triple CIC device to both a sinusoidal and a square wave AC current of  $I_{rms} = 8$  mA. Any resonant frequency differences between the two excitation wave shapes are not considered significant. No sinusoidal resonances were observed below 13.2 kHz, whereas the square wave excitation apparently produces several. This can be explained by considering the expansion of a symmetric unit square wave  $f(t)$  at frequency  $\omega$  as a Fourier series:

$$f(t) = \frac{4}{\pi} \sum_{n=0}^{\infty} \frac{\sin((2n+1)\omega t)}{(2n+1)}.$$

We thus would expect to observe a square-wave resonance for some  $n$  whenever  $(2n+1)\omega$  is a resonant frequency for the sinusoidal excitation. This is observed for  $n = 1$  and 2 and  $(2n+1)\omega$  is either the fundamental or the second harmonic. The magnitude of each of

the harmonics is scaled accordingly by the factor  $\frac{4}{\pi} \frac{1}{(2n+1)}$ .

For example, we observed with a photodiode that resonance no. 4 listed in Table 1 is actually oscillating at three times the applied square wave frequency. This corresponds closely to the sine wave frequency of resonance no. 7. The frequencies of all of the

Table 1  
Resonant frequencies of a triple CIC device.

Resonance No.	Square-wave AC Excitation		Sinusoidal AC Excitation		Simulation
	Frequency (kHz)	Deflection (°)	Frequency (kHz)	Deflection (°)	Frequency (kHz)
1	2.23	5			
2	3.20	6			
3	4.45	5			
4	5.23	9			
5	7.30	3			
6	13.20	11	13.23	10	13.0
7	15.90	27	16.03	21	17.2
8	34.60	(orthogonal)	34.34	(orthogonal)	34.0
9	35.50	8	36.46	6	
10	56.80	4	56.78	4	

resonance nos. 1–5 correspond to odd submultiples of sinusoidal resonance nos. 6, 7 or 9. Even the angular deflections roughly scale according to the above factor.

The small resonance near 34.5 kHz labeled *orthogonal* indicates an oscillation that was in the direction orthogonal to the other oscillations, and represents a lateral vibration. The frequency corresponds closely to the simulated orthogonal resonance. Its excitation, when the Lorentz force has no component in the orthogonal direction, may be caused by the slight asymmetry in the metal leads of the device; the metal1 to metal2 via is on the arm of the cantilever (see Fig. 2(b)) rather than at the end of the cantilever, producing a center of mass of the device that is slightly off the geometric line of symmetry.

The frequencies of the largest resonance indicated in Fig. 5 and Table 1 are not equal; they were obtained from two different triple CIC devices. This difference is presumably due to fabrication process variations.

An interesting phenomenon associated with the Joule heating in the Al leads occurs at resonance. We measured the resistance of the leads of the triple CIC structure used to generate the data of Table 1 as it was driven through resonance by a 10 mA AC square wave at 15.9 kHz, and obtained the average temperature of the support arms. The temperature decreased by 0.5°C at resonance, due to, we surmise, the large oscillations of the center cantilever producing a cooling effect in the ambient air. The average temperature increase is plotted as a function of frequency in Fig. 6, showing clearly the decrease in the temperature as resonance is reached. We suspect the temperature at frequencies below resonance is lower than that above resonance because there is another resonance near 13 kHz, as indicated in Table 1.

We also operated a triple device at resonance for  $2.5 \times 10^{10}$  cycles (17 days) and observed no change in the deflection characteristics. Thus, we expect a high degree of reliability in operation of these devices.

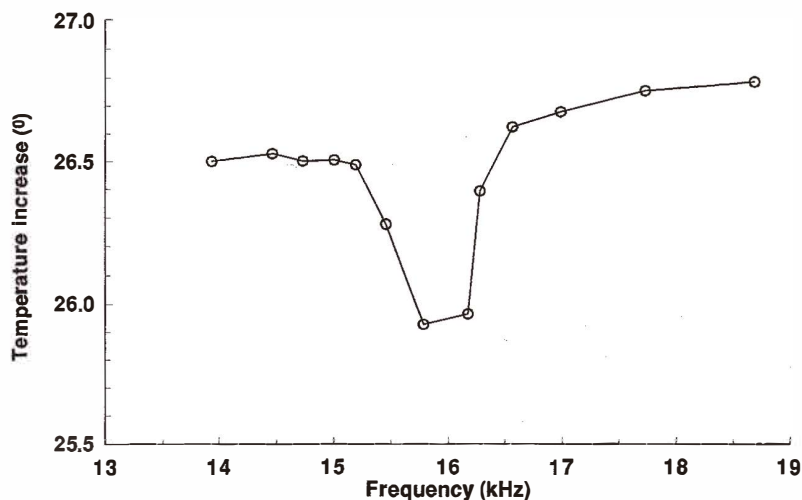


Fig. 6. Temperature increase of the cantilever arms versus frequency for a triple CIC device.

#### 6.4 Simulations

The simulated static deflection of our structure is shown in Fig. 7, where the outer cantilever arms are clamped to the substrate to the right in the diagram. The scale of the z-axis is  $10^{-2}$  that of the other two axes. The first three relevant resonant modes are listed in Table 1, for comparison with the experimental results. The simulation results for the first two normalized resonant modes are shown in Figs. 8(a) and 8(b). These plots, plus some elementary geometric considerations, were employed to calculate the damping term  $\rho_1$ . A simple calculation shows that the component of the resulting load due to the Lorentz force in the structure is greater for the second resonant mode than for the first. Since the damping is also less for the second eigenvector due to the node being located at the midpoint of the mirror, the deflection is greater at the second resonant mode, for both the experimental and simulated results, than for the fundamental. The device response as a function of frequency about the second resonance is shown in Fig. 9, where a comparison with the experiment is also obtained. Considering the fabrication process variations for the actual device, and the uncertainties in the material properties and geometric values in the simulations, the agreement between the two curves is quite reasonable. We emphasize that the simulation results were based on the design specifications. Accurate knowledge of the geometric and physical parameters and of the damping term for the specific device being simulated would presumably yield better agreement.

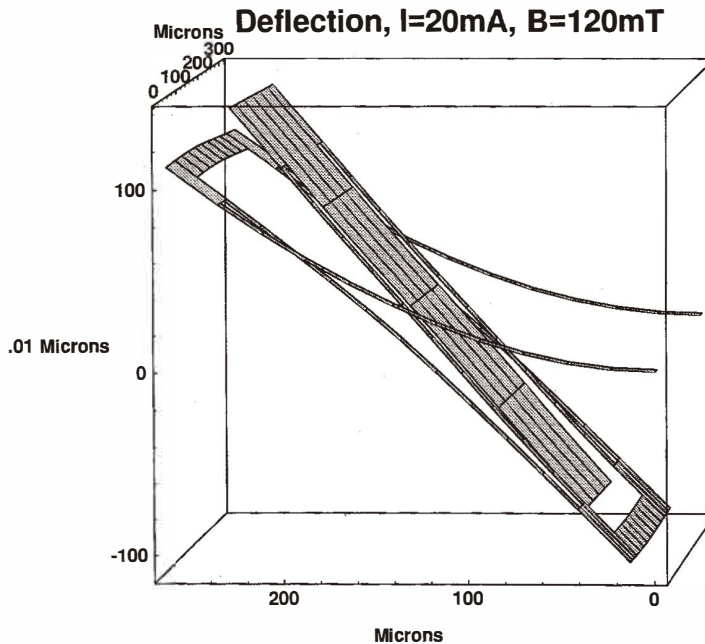


Fig. 7. Simulated displacements of a triple CIC under static conditions.

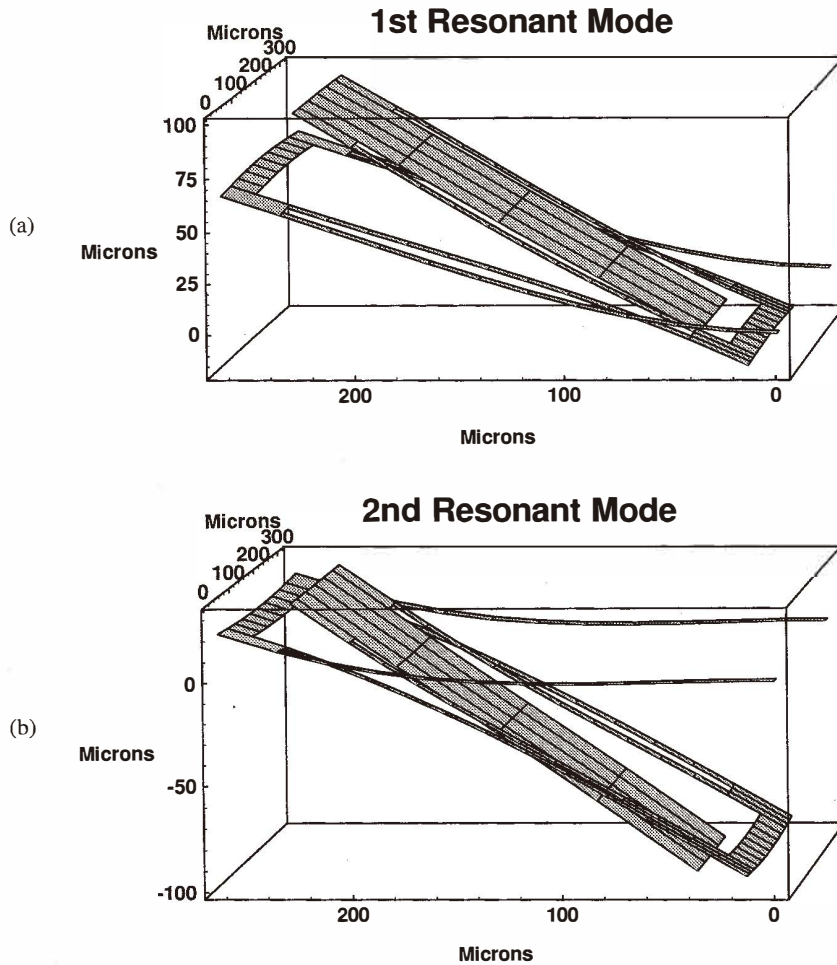


Fig. 8. (a) Simulated maximum displacement at the first resonant mode. (b) Simulated maximum displacement at the second resonant mode.

The simulation results show that the third observed resonant mode is transverse to the other two; and given the nature of the applied load, the deflection is quite small. This shows one of the characteristics of the specific device; namely that large deflections only occur for the orientation of the device and magnetic field employed in this paper. If the magnetic field is rotated by  $90^\circ$ , much less deflection is observed due to the increased rigidity of the structures to the effect of the newly oriented Lorentz forces.

Finally, in Fig. 10, we indicate the simulated shift in the second resonant mode due to

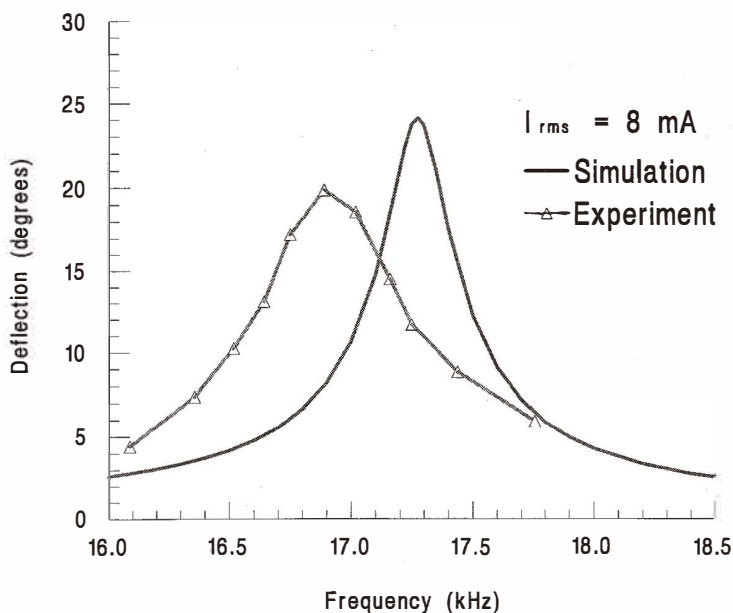


Fig. 9. Comparison of experimental and simulated resonance response for a triple CIC device.

increasing the thickness of the nitride layer by  $0.1 \mu\text{m}$  throughout the device. We observe that the shift is approximately  $1.2 \text{ kHz}$ , while the increase in the device mass due to the increased thickness is approximately  $1.6 \text{ ng}$ . From this simulation we conclude that this device can potentially be used to measure mass changes of the order of  $1 \text{ ng}$ , which is comparable to the results obtained by the related methods referred to previously.<sup>(10,19)</sup>

## 7. Conclusions

We have presented the fabrication and simulation of a magnetically actuated device constructed using a standard CMOS process. The structure involves a cantilever-in-cantilever design to enhance angular displacement.

The incorporation of piezoresistive materials to determine the resonant mode, rather than the optical approach presently used, and of magnetic strips on the chip to replace the external magnets, is presently being investigated.

## Acknowledgments

We gratefully acknowledge the services of the Canadian Microelectronics Corporation and Northern Telecom Canada Ltd. in the fabrication of the devices used in this work. We

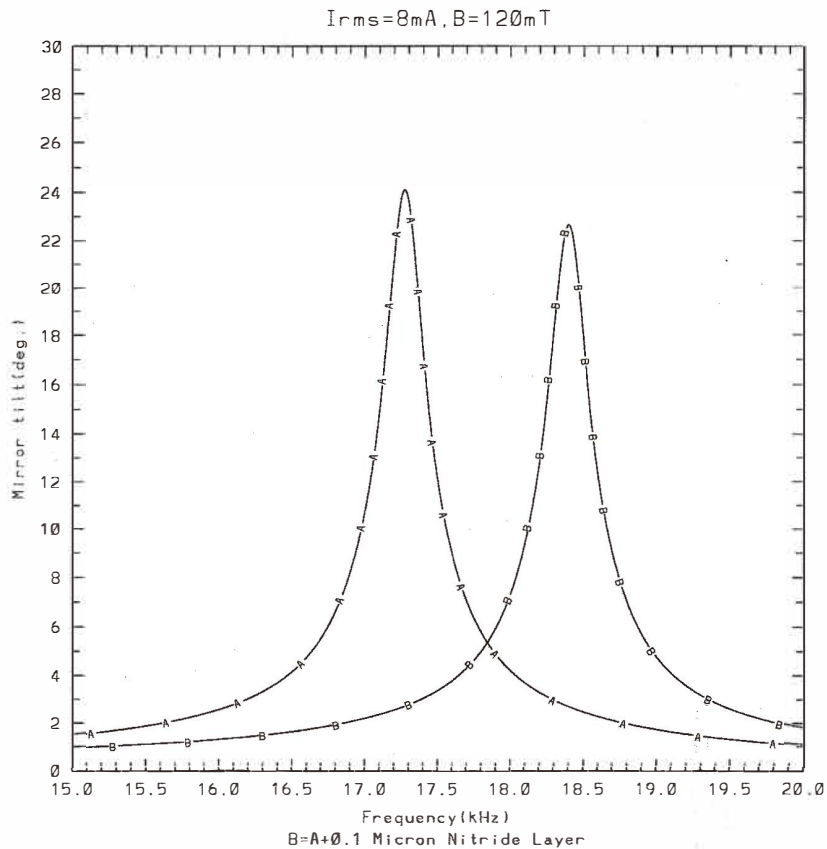


Fig. 10. Simulated resonance curves of a triple CIC device with standard nitride layer (curve A) and with nitride layer increased by  $0.1 \mu m$  (curve B).

thank T. M. Hrudey of the Civil Engineering Department, who assisted us with the derivation of the static analytic equations. Thanks are also given for the assistance of R. Haley of the EE Department and the staff at the Alberta Microelectronic Centre. This work was partially supported by the Natural Sciences and Engineering Research Council of Canada.

### References

1. M. Parameswaran, H. P. Baltes and A. M. Robinson: IEEE Solid-State and Actuators Workshop Digest of Technical Papers 1988 (IEEE New York, 1988) p. 148.

- 2 M. Parameswaran, Lj. Ristic, A. C. Dhaded and H. P. Baltes: Proc. Canadian Conf. Electrical and Comp. Eng. 1988 (Vancouver, 1988) p.781.
- 3 M. Parameswaran, H. P. Baltes, Lj. Ristic, A. C. Dhaded and A. M. Robinson: *Sensors and Actuators* **19** (1989) 298.
- 4 M. Parameswaran, Lj. Ristic, A. C. Dhaded, H. P. Baltes, W. Allegretto and A. M. Robinson: *Can. J. Phys.* **67** (1989) 184.
- 5 M. Parameswaran: PhD Thesis 1990 (University of Alberta).
- 6 M. Parameswaran, A. M. Robinson, Lj. Ristic, K. Chau and W. Allegretto: *Sensors and Actuators B* **2** (1990) 17.
- 7 M. Parameswaran, A. M. Robinson, D. L. Blackburn, M. Gaitan and J. Geist: *IEEE Electron Devices Letters* **12** (1991) 57.
- 8 D. Moser, O. Brand and H. Baltes: *Transducers '91* (IEEE, New York, 1991) p. 547.
- 9 A. M. Robinson, P. Haswell, R. P. W. Lawson and M. Parameswaran: *Rev. Sci. Instrum.* **63** (1992) 2026.
- 10 S. Prescesky, M. Parameswaran, A. Rawicz, R. F. B. Turner and U. Reichl: *Can. J. Phys.* **70** (1992) 1178.
- 11 R. Lenggenhager, H. Baltes, J. Peer and M. Forster: *IEEE Electron Device Letters* **EDL-13** (1992) 454.
- 12 G. H. Chapman, M. Parameswaran and M. J. Szyrzycki: *Int. Conf. on Wafer Scale Integration Proceedings* (San Francisco, 1992) p. 300.
- 13 M. Parameswaran and M. Paranjape: *Sensors and Materials* **5** (1993) 113.
- 14 M. Paranjape: PhD Thesis 1993 (University of Alberta, 1993).
- 15 O. Brand, H. Baltes and U. Baldenweg: *IEEE Trans. Electron Devices* **40** (1993) 1745.
- 16 R. Lenggenhager, H. Baltes and T. Elbel: *Sensors and Actuators A* **37-38** (1993) 216.
- 17 N. R. Swart and A. Nathan: *Sensors and Actuators A* **43** (1994) 3.
- 18 B. Shen, Z. Lai, A. M. Robinson and W. Allegretto: *Rev. Sci. Instrum.* **65** (1994) 3528.
- 19 J. M. Chen and M. Parameswaran: *Seventh Can. Semiconductor Technology Conf.* (Ottawa, 1995).
- 20 I. Stiharu, L. Landsberger and M. Paranjape: *Seventh Can. Semiconductor Technology Conf.* (Ottawa, 1995).
- 21 E. Hoffman, B. Warneke, E. Kruglick, J. Weigold and K. S. J. Pister: *IEEE MEMS Workshop* (Amsterdam, 1995) p. 288.
- 22 E. J. J. Kruglick, S. Damle and K. S. J. Pister: *Proc. SPIE Conf. Micromachined Devices and Components* (Austin, TX, Oct., 1995) p. 33.
- 23 J. S. Suehle, R. E. Cavicchi, M. Gaitan and S. Semancik: *IEEE Electr. Dev. Letts.* **14** (1993) 118.
- 24 R. E. Cavicchi, J. S. Suehle, K. G. Kreider, M. Gaitan and P. Chararala: *IEEE Electr. Dev. Letts.* **16** (1995) 286.
- 25 J. Bühler, J. Funk, O. Paul, F.-P. Steiner and H. Baltes: *Sensors and Actuators A* **46-47** (1995) 572.
- 26 J. Funk, J. Bühler, J. G. Korvink and H. Baltes: *Sensors and Actuators A* **46-47** (1995) 632.
- 27 F. P. Beer and E. R. Johnston: *Mechanics of Materials* (McGraw-Hill Ryerson, Toronto 1985).
- 28 B. Shen: PhD Thesis (University of Alberta, 1996).
- 29 S. Timoshenko and S. Woinowsky-Krieger: *Theory of Plates and Shells* (McGraw-Hill, NY 1959).
- 30 G. Strang and G. Fix: *An Analysis of the Finite Element Method* (Prentice-Hall, NY 1973) p. 83.